Nonlinear Compliant Modes for Large-Deformation Analysis of Flexible Structures

SIMON DUENSER, ETH Zurich, Switzerland
BERNHARD THOMASZEWSKI, ETH Zurich, Switzerland
ROI PORANNE, University of Haifa, Israel and ETH Zurich, Switzerland
STELIAN COROS, ETH Zurich, Switzerland

Many flexible structures are characterized by a small number of *compliant modes*, i.e., large deformation paths that can be traversed with little mechanical effort, whereas resistance to other deformations is much stiffer. Predicting the compliant modes for a given flexible structure, however, is challenging. While linear eigenmodes capture the small-deformation behavior, they quickly divert into states of unrealistically high energy for larger displacements. Moreover, they are inherently unable to predict nonlinear phenomena such as buckling, stiffening, multistability, and contact. To address this limitation, we propose *Nonlinear Compliant Modes*—a physically-principled extension of linear eigenmodes for large-deformation analysis. Instead of constraining the entire structure to deform along a given eigenmode, our method only prescribes the projection of the system's state onto the linear mode while all other degrees of freedom follow through energy minimization. We evaluate the potential of our method on a diverse set of flexible structures, ranging from compliant mechanisms to topology-optimized joints and structured materials. As validated through experiments on physical prototypes, our method correctly predicts a broad range of nonlinear effects that linear eigenanalysis fails to capture.

CCS Concepts: • **Applied computing → Computer-aided design**; • **Computing methodologies → Physical simulation**; **Continuous simulation**.

Additional Key Words and Phrases: computational design, elasticity, characteristic deformation, non-linearity, physical simulation, finite element method

ACM Reference Format:
Simon Duenser, Bernhard Thomaszewski, Roi Poranne, and Stelian Coros. 2022. Nonlinear Compliant Modes for Large-Deformation Analysis of Flexible Structures. *ACM Trans. Graph.* 42, 2, Article 21 (October 2022), 11 pages. https://doi.org/10.1145/3568952

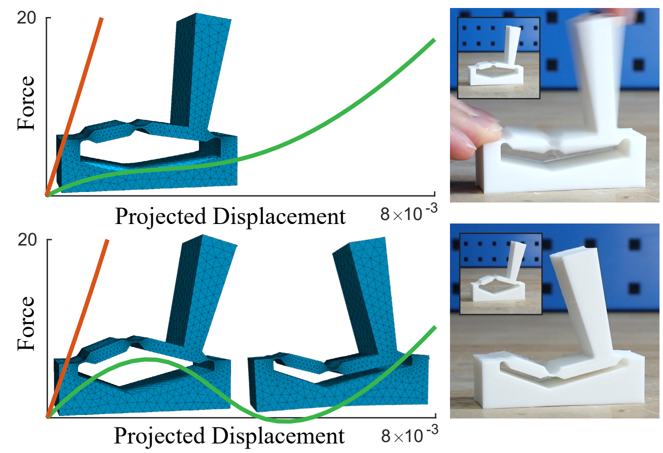

Fig. 1. Designing a compliant switch. While linear eigenanalysis identifies switch activation as a compliant direction for an initial design (*top row*), it is inherently unable to predict nonlinear effects such as bistability. Our method computes nonlinear continuations of the linear eigenmodes for the entire range of motion of the switch, revealing that the initial design does not exhibit a second equilibrium state (*top row*, *green curve*). An improved design (*bottom row*) with marginally larger travel for the center flexure maintains lateral stiffness (*red curve*) while achieving the desired bistability (*green curve*).

1 INTRODUCTION

Understanding and designing flexible structures that undergo large deformations is a challenging problem. For small displacements, linear eigenanalysis offers a succinct description of a mechanical system through a set of eigenmodes that characterize its behavior in a physically meaningful way. This linearity assumption is warranted in engineering problems for which preventing large deformations is a central goal. Flexible metamaterials, compliant mechanisms, and elastic joints, however, are examples that undergo large deformations by design. In this finite-deformation setting, linear eigenmodes rapidly become inadequate as they predict deformations with unrealistically high energy. Furthermore, linear modes are inherently unable to capture nonlinear effects such as stiffening, buckling, and multistability, all of which are phenomena frequently encountered in flexible structures.

While the problem of nonlinear characterization and modeling of *local* material properties is well studied, there is no formal framework for analyzing the *global* interplay between geometry, material, and mechanics. Nonlinear finite element solvers are able to predict the compliant behavior in principle, but defining the right forcing functions is very challenging, in particular for geometrically complex models, and requires expert knowledge.

To address this problem, we propose a formulation that extends linear eigenmodes to the nonlinear regime of large deformations in a natural and physically principled way: instead of constraining the entire structure to deform along a given eigenmode, our method only prescribes the projection of the system's state onto the linear eigenmode—all other degrees of freedom follow through energy minimization in the orthogonal subspace. The resulting nonlinear

This research was supported by the Swiss National Science Foundation through the National Centre of Competence in Digital Fabrication (NCCR DFAB) and through Grant No. 200021 200644, and by the European Research Council (ERC) under the European Union's Horizon 2020 research and innovation program (Grant No. 866480).
Authors' addresses: Simon Duenser, ETH Zurich, Switzerland, simon.duenser@inf.ethz.ch; Bernhard Thomaszewski, ETH Zurich, Switzerland; Roi Poranne, University of Haifa, Israel and ETH Zurich, Switzerland; Stelian Coros, ETH Zurich, Switzerland.

compliant modes coincide with the linear eigenstructure at the origin while extending it in an energetically optimal way for larger deformations. The variational viewpoint we present directly leads to a constrained optimization problem, allowing us to leverage well established numerical solution methods. We thus arrive at an effective and robust algorithm for computing nonlinear compliant modes characterized by buckling, stiffening, multistability, and other forms of nonlinearity.

We analyze our method on a diverse set of flexible structures ranging from compliant mechanisms to topology-optimized joints and structured materials. We additionally validate our simulation results through experiments on physical prototypes. Our findings indicate that our method is able to correctly predict a broad range of nonlinear effects that linear eigenanalysis fails to capture.

2 RELATED WORK

Designing for Flexibility. The graphics community has in recent years seen an increasing interest in computational design tools for flexible structures [Guseinov et al. 2017; Megaro et al. 2017; Panetta et al. 2017; Pérez et al. 2017; Skouras et al. 2014] and materials [Malomo et al. 2018; Martínez et al. 2016, 2019; Panetta et al. 2015; Schumacher et al. 2018]. Like our research, many of these efforts target designs that exhibit large elastic deformations. However, while each of them solves a specific design problem for a well-defined parameter space and known inputs, we address the fundamental and general question of how to characterize the finite-deformation behavior of flexible structures from shape and material descriptions.

Despite their limitation for large deformations, linear eigenmodes have proven useful for several applications in the field of computational fabrication. One line of work leverages resonance simulation or eigenmode optimization for designing physical artifacts with desired sound properties [Bharaj et al. 2015; Musialski et al. 2016; Umetani et al. 2010, 2016]. Another application is for analyzing and optimizing the stability of designs 3D-printed with materials that fail beyond the small-deformation regime [Zhou et al. 2013]. In a similar spirit, Zehnder et al. [2016] detect unwanted structural flexibility in ornamental curve networks using sparse linear eigenanalysis.

While the above methods target the small-deformation regime, an exception to this rule is the recent work by Tang et al. [2020] for designing nonlinear elastic systems with large-amplitude oscillations. However, while Tang et al. focus on dynamic, periodic motion, our goal is to find large deformations in static equilibrium.

Subspaces for Physics-Based Modeling & Simulation. Although our goal is not to create subspaces, our method shares some concepts that have proven useful for reduced simulation. An approach that is widely used in engineering for vibration problems is linear modal analysis (LMA) [Shabana 1990]. In essence, LMA computes a low-dimensional linear basis by solving a generalized eigenvalue problem involving energy Hessian and mass matrix of a discrete elastic system and discarding eigenvectors beyond the spectrum of interest. While this approach is efficient and effective for small deformations, the limitations of truncated linear eigenbases for larger deformations are well known and documented; see, e.g., [Hildebrandt et al. 2011] for a discussion.

Many different strategies have been suggested in order to mitigate the limitations of linear eigenmodes in the finite-deformation regime while preserving their predictive power for small deformations. Notable examples include the addition of eigenmode derivatives [Barbič and James 2005], modal deformations [von Tycowicz et al. 2013], or higher-order descent directions [Hildebrandt et al. 2011], adaptive replacement of eigenvectors [Hahn et al. 2014; Kim and James 2009], and correction of linearization artefacts [Barbič et al. 2012; Pan et al. 2015]. As one particular example, Choi and Ko [2005] propose modal warping as a means to alleviate artifacts of linear modes due to rotations. With a similar motivation, Huang et al. [2011] propose rotation strain extrapolation to reduce linearization artifacts. While offering improvements in visual quality for animation purposes, *neither modal warping nor rotation-strain extrapolation are physically accurate* since they rely on geometry-reconstruction steps that are not physically motivated.

While most works aim at constructing efficient linear subspaces, a notable exception is the recent work by Fulton et al. [2019] who infer nonlinear subspaces from full-space simulation data using machine learning. Holden et al. [2019] follow a similar idea but learn nonlinear corrections for linearized cloth deformations. As a conceptual link, our nonlinear eigenmodes can likewise be considered nonlinear corrections to their linear counterparts. However, whereas Holden et al. approximate corrections based on data, they emerge as the solution to a constrained energy minimization problem in our formulation.

As a core component of our approach, the concept of defining nonlinear motion by minimizing energy orthogonal to a given subspace has also been used successfully in animation, e.g., for augmenting artist-created animations with simulation-based secondary motion within [Hahn et al. 2012] or orthogonal to [Zhang et al. 2020] a given rig-space, or for example-based simulation of elastic materials [Martin et al. 2011].

Nonlinear Normal Modes. The study of vibrations is a central problem in many engineering disciplines. But whereas the linear theory for small deformations is well understood, the generalization to the nonlinear setting is far from obvious and there are many different concepts that can collectively be referred to as nonlinear normal modes. While an exhaustive review of this field is beyond the scope of this work, we mention here two main directions on which much of the existing literature builds: Rosenberg's principle of synchronous oscillation [1966], and the concept of invariant manifolds due to Shaw and Pierre [1991; 1993]. While our problem setting (statics vs. dynamics) and formulation (implicit definition vs. explicit approximation) are very different, we draw inspiration from the core idea of Shaw and Pierre: we obtain nonlinear compliant modes by parameterizing our flexible structures by a single generalized coordinate—all remaining degrees of freedom follow from the governing principle of energy minimization.

3 THEORY

To set the stage for nonlinear compliant modes, we start by reviewing linear eigenmodes in the small deformation setting (Sec. 3.1). We then introduce a variational view on eigenmodes (Sec. 3.2) that

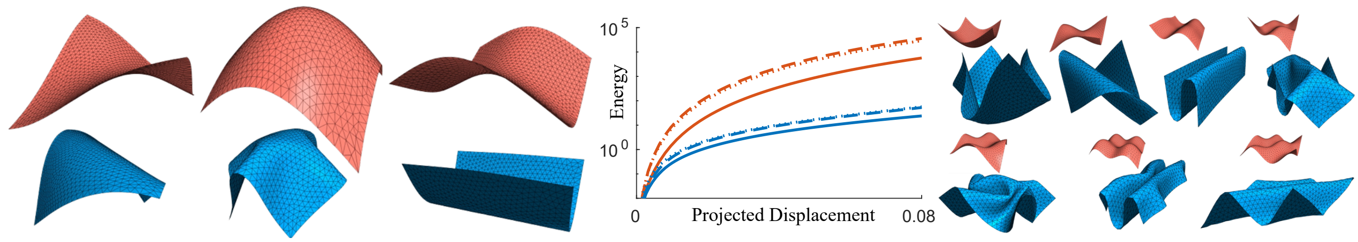

Fig. 2. *Left*: Comparison between the first three linear modes (*red*) and our nonlinear compliant modes (*blue*) on a thin sheet. *Middle*: energy as a function of displacement projected along the eigenmode for the first three modes (*solid, dashed* and *dotted* lines, in order) . *Right*: additional modes with increasing stiffness.

serves as the basis for our nonlinear formulation, which we develop in Sec. 3.3.

3.1 Linear Eigenmodes

Consider a discrete mechanical system represented through n nodes, with $\mathbf{x} \in \mathbb{R}^{3n}$ and $\mathbf{X} \in \mathbb{R}^{3n}$ describing its current and reference configurations, respectively. Let $E(\mathbf{x};\mathbf{X})$ denote the discrete elastic energy, $\mathbf{f} = -\nabla E$ the corresponding internal forces, and $\mathbf{H} = \nabla^2 E$ its Hessian. For later use, we also introduce the displacement vector $\mathbf{u} = \mathbf{x} - \mathbf{X}$. The linear eigenspace of $\mathbf{H}$ is a set of $3n$ eigenvectors $\mathbf{e}_i \in \mathbb{R}^{3n}$ with corresponding eigenvalues σ_i that are obtained by solving the symmetric eigenvalue problem[1]

$$\mathbf{H}\mathbf{e}_i = \sigma_i \mathbf{e}_i \quad , \quad \mathbf{e}_i^\mathsf{T} \mathbf{e}_j = \delta_{ij} \; . \tag{1}$$

A physical interpretation of this eigenstructure can be obtained using a quadratic expansion of the energy. For sufficiently small displacements $\mathbf{u}$ around the origin, we have

$$E(\mathbf{X}+\mathbf{u}) = E(\mathbf{X}) - \mathbf{f}(\mathbf{X})^\mathsf{T}\mathbf{u} + \frac{1}{2}\mathbf{u}^\mathsf{T}\mathbf{H}\mathbf{u} = \frac{1}{2}\mathbf{u}^\mathsf{T}\mathbf{H}\mathbf{u} \, , \tag{2}$$

and, consequently, $\mathbf{f}(\mathbf{X}+\mathbf{u}) = -\mathbf{H}\mathbf{u}$. In particular, when choosing a displacement $\mathbf{u}(t) = t\mathbf{e}_i$ along an eigenvector, we see that $\mathbf{H}\mathbf{u}(t) = t\sigma_i\mathbf{e}_i$ describes a force collinear with the displacement from which it stems. While this force-displacement collinearity along eigenmodes is a charateristic property for small displacements, it cannot be expected to hold for nonlinear forces and finite displacements. However, a reformulation of this condition provides opportunities for generalization.

3.2 Variational View

Consider the constrained optimization problem

$$\min_{\mathbf{u}} E(\mathbf{X}+\mathbf{u}) \quad \text{s.t.} \quad \mathbf{e}_i^\mathsf{T}\mathbf{u} = t \, , \tag{3}$$

for an arbitrary but fixed displacement magnitude t and a given eigenmode $\mathbf{e}_i$. The corresponding Lagrangian is

$$\mathcal{L} = E(\mathbf{X}+\mathbf{u}) - \lambda(\mathbf{e}_i^\mathsf{T}\mathbf{u} - t) \tag{4}$$

where λ is a Lagrange multiplier. The first-order optimality conditions are

$$\nabla_\mathbf{u}\mathcal{L} = \nabla E(\mathbf{X}+\mathbf{u}) - \lambda\mathbf{e}_i = -\mathbf{f}(\mathbf{X}+\mathbf{u}) - \lambda\mathbf{e}_i \; = \mathbf{0} \, , \tag{5}$$

$$\nabla_\lambda\mathcal{L} = t - \mathbf{e}_i^\mathsf{T}\mathbf{u} = 0 \; . \tag{6}$$

For small displacements we have $-\mathbf{f}(\mathbf{X}+\mathbf{u}) = \mathbf{H}\mathbf{u}$ and, since $\mathbf{H}$ is positive definite at the origin, the above optimization problem is a convex quadratic program with a unique solution $\mathbf{u} = t\mathbf{e}_i$. Consequently, we see that linear modes $\mathbf{u}_i(t) = t\mathbf{e}_i$ are minimizers of elastic energy subject to modal displacement constraints. This observation provides a direct opportunity for nonlinear generalization.

3.3 Nonlinear Compliant Modes

Motivated by the variational view on linear eigenmodes expressed through (3–6), we define nonlinear compliant modes as

$$\mathbf{n}_i(t) = \mathbf{X} + \arg\min_{\mathbf{u}} E(\mathbf{X}+\mathbf{u}) \quad \text{s.t.} \quad \mathbf{e}_i^\mathsf{T}\mathbf{u} = t \; . \tag{7}$$

This formulation ensures that nonlinear compliant modes correspond to linear eigenmodes at the origin while extending them in an energetically optimal way for larger deformations. Another perspective is obtained when rewriting (7) as

$$\mathbf{n}_i(t) = \mathbf{l}_i(t) + \arg\min_{\mathbf{y}} E(\mathbf{l}_i(t)+\mathbf{y}) \quad \text{s.t.} \quad \mathbf{e}_i^\mathsf{T}\mathbf{y} = 0 \, , \tag{8}$$

where $\mathbf{l}_i(t) = \mathbf{X} + t\mathbf{e}_i$ denotes displacement along the *linear* eigenmode. This shows that nonlinear compliant modes follow a prescribed displacement along their corresponding linear eigenmode while minimizing the elastic energy in the space orthogonal to it. The displacement $\mathbf{y} = \mathbf{n}_i - \mathbf{l}_i$ can be interpreted as a nonlinear correction to the linear eigenmode.

Unlike for small displacements, convexity cannot be guaranteed for finite deformations due to the nonlinearity of E. As explained below, we deal with potential indefiniteness by requiring that points along $\mathbf{n}_i$ always correspond to true minimizers, not merely saddle points. The reasoning behind this strategy is that, whereas constrained minimizers are locally stable configurations, saddle points correspond to unstable equilibria that are unlikely to occur in physical reality.

3.4 Algorithm

We compute nonlinear compliant mode i by solving (7) for discrete values of $t = t_j \in \mathbb{R}$, $t_j \in [0, t_1, \ldots, t_{\max}]$ with $t_{j+1} > t_j$, yielding

[1] To simplify the exposition, we focus on the eigenvectors of $\mathbf{H}$ with orthogonality conditions based on the canonical Euclidean metric. In practice, however, we enforce mass-orthogonality among eigenvectors to achieve resolution-independent weighting of individual nodes, leading to generalized eigenvectors computed through a generalized eigenvalue problem.

a set of samples $\mathbf{n}_{i,j}$. To this end, we employ Newton's method in conjunction with standard line-search. Using (5) and (6) we can directly find the first-order (necessary) conditions for (7), i.e.,

$$\nabla E(\mathbf{n}_i(t)) - \lambda(t)\,\mathbf{e}_i \;= \mathbf{0}\,, \tag{9}$$

$$\mathbf{e}_i^\top(\mathbf{n}_i(t) - \mathbf{X}) - t = 0\,. \tag{10}$$

Here we stress the dependence of the Lagrange multiplier on the mode parameter, i.e. $\lambda = \lambda(t)$. For any time step t_j we find the pair $(\mathbf{n}_{i,j}, \lambda_j)$ through Newton's method. For each iteration k, we first compute a search direction by solving the linearized first-order optimality conditions,

$$\begin{bmatrix} \mathbf{H}(\mathbf{n}_{i,j}^k) & -\mathbf{e}_i \\ -\mathbf{e}_i^\top & 0 \end{bmatrix} \begin{bmatrix} \Delta\mathbf{n}^k \\ \Delta\lambda^k \end{bmatrix} = \begin{bmatrix} -\nabla E(\mathbf{n}_{i,j}^k) + \lambda_j^k \mathbf{e}_i \\ \mathbf{e}_i^\top(\mathbf{n}_{i,j}^k - \mathbf{X}) - t \end{bmatrix}\,. \tag{11}$$

We then use a backtracking line-search to find a configuration $\mathbf{n}_{i,j}^{k+1} = \mathbf{n}_{i,j}^k + \beta\Delta\mathbf{n}^k$ for $0 < \beta < 1$ that yields a sufficient decrease in the merit function

$$\phi(\mathbf{x};\mu) = E(\mathbf{x}) + \mu\,|\mathbf{e}_i^\top(\mathbf{x} - \mathbf{X}) - t|\,. \tag{12}$$

Likewise, the Lagrange multiplier λ_j^{k+1} is updated with $\beta\,\Delta\lambda^k$. To determine the constraint coefficient μ, we first compute

$$\mu^k = \frac{\nabla E^k \Delta\mathbf{n}^k + \frac{1}{2}\Delta\mathbf{n}^{k^\top}\mathbf{H}^k\Delta\mathbf{n}^k}{0.5\,|\mathbf{e}_i^\top(\mathbf{n}^k - \mathbf{X}) - t|}\,, \tag{13}$$

and then set $\mu = \max(\mu^{k-1}, \mu^k)$; see [Nocedal and Wright 2006], Eq. (18.36). If necessary, we re-solve system (11) with exponentially increasing diagonal regularization on $\mathbf{H}$ until $\Delta\mathbf{n}^{k^\top}\,\mathbf{H}\,\Delta\mathbf{n}^k > 0$, which ensures that $\Delta\mathbf{n}^k$ is a descent direction for ϕ [Nocedal and Wright 2006].

Discrete Steps. To compute a nonlinear mode we solve system (9-10) for a sequence of discrete steps t_j with uniform step size. The main consideration in choosing the step size is to achieve sufficient resolution to interpret the resulting force- and stiffness plots, or examine the corresponding motion of the object. When solving for $\mathbf{n}_i(t_j)$ we initialize the algorithm with the previous step $\mathbf{n}_i(t_{j-1})$, which speeds up computation if the two configurations are close. It should further be noted that the eigenvectors $\mathbf{e}_i$ are not unique, but only defined up to the sign. To explore both cases, one can equivalently use a sequence of $t_j < 0$.

Excluding Rigid Motion. If no boundary conditions are imposed, $\mathbf{H}(\mathbf{X})$ has a six-dimensional null-space corresponding to rigid body transformations. This is a direct consequence of the elastic energy's invariance to translation and rotation. Away from the origin, however, the null-space only consists of translations, since non-zero forces are not invariant under rotations. To remove all potential singularities due to rigid motion, we ask that $\sum_l \Delta n_l^k = \mathbf{0}$ and $\sum_l \left(X_l \times \Delta n_l^k\right) = \mathbf{0}$, where Δn_l^k, $X_l \in \mathbb{R}^3$ are segments of $\Delta\mathbf{n}^k$ and $\mathbf{X}$ that correspond to node l. These conditions are enforced by adding the corresponding constraint gradients to system (11).

Mass Orthogonality & Normalization. To minimize the dependence of eigenmodes on the specific choice of discretization, we replace the canonical dot product in (1) with a corresponding mass-orthogonality condition, $\mathbf{e}_i^\top\mathbf{M}\mathbf{e}_j = \delta_{ij}$, using a diagonalized mass matrix $\mathbf{M}$. We then solve the generalized symmetric eigenvalue problem $\mathbf{He} = \sigma\mathbf{Me}$ as described in Sec. 4.7. The diagonal elements of $\mathbf{M}$ represent the lumped mass of the node corresponding to each degree of freedom, whereby the total mass of the structure is normalized to one. Accordingly, also the inner product of the linear constraint in (7) is weighted and becomes $\mathbf{e}_i^\top\mathbf{M}\mathbf{u} = t$, such that t can be seen as an average displacement of the structure along the normalized eigenmode. We will refer to this measure as the *projected displacement.*

Local Restriction. Although prescribing displacement along a linear eigenmode $\mathbf{l}(t)$ removes only one degree of freedom from the system, it generally affects all nodes in the mesh. In practice, however, it can be desirable to restrict locations at which displacement can be prescribed to specific *active* regions such as the boundary of the mesh. By enforcing the displacement constraint only for specific components of the linear eigenmode, our formulation can be extended to support this localization in a straightforward manner; see Appendix A.

3.5 Discussion

Invariant Manifolds. As is evident from (7), our formulation prescribes the system's state along one generalized coordinate—a linear eigenmode—while the remaining degrees of freedom follow from the governing physical principles. This concept is similar to, and indeed inspired by, the seminal work by Shaw and Pierre [1991] on nonlinear normal modes, who construct their modes by *local approximation* of *invariant manifolds* arising from the equations of motion. In contrast to this and other approaches using localized invariant manifolds for characterizing dynamic systems (see e.g. [Jain and Haller 2022]), we investigate *quasi-static* systems. Furthermore, through minimization of energy each individual point on our nonlinear compliant modes is defined implicitly, enabling efficient *global* computation. Global computation of invariant manifolds of dynamic systems, on the other hand, remains a major challenge for high-dimensional systems [Jain and Haller 2022], in part because they generally do not offer such an implicit definition and must be evolved from a known starting point [Krauskopf et al. 2005].

Physical Interpretation. An important benefit of the proposed nonlinear modes lies within the intuitive physical interpretation they offer. The first-order optimality condition (9) can be viewed as the equilibrium condition for an elastic system subject to an external force $\mathbf{f}^{\text{ext}}(t) = \lambda(t)\mathbf{e}_i$. This observation suggests that a configuration $\mathbf{n}_i(t)$ can be reached simply by applying a force with direction $\mathbf{e}_i$ and magnitude $\lambda(t)$ to the system. We call this a *modal force* . However, to obtain a full picture of the physical behaviour of an elastic system, it is indispensable to also consider stability. It is easy to verify that the first-order optimality conditions (9) are shared with a similar, but unconstrained system defined by the potential energy $E(\mathbf{x}) + \mathbf{x}^\top\mathbf{f}^{\text{ext}}$. The well established conditions for stable equilibrium in this case are $\mathbf{H}(\mathbf{x}) \succ 0$, i.e., the Hessian must be positive definite [Eriksson and Nordmark 2019]—which is simply the second-order optimality condition for the unconstrained minimization problem

$$\min_{\mathbf{x}} E(\mathbf{x}) + \mathbf{x}^{\mathsf{T}}\mathbf{f}^{\text{ext}} . \tag{14}$$

In comparison, the second-order optimality condition for (7) can be expressed as

$$\mathbf{p}^{\mathsf{T}}\ \mathbf{H}(\mathbf{x})\ \mathbf{p} \geq 0 \qquad \forall \mathbf{p} \in \mathbb{R}^{3n},\ \|\mathbf{p}\| > 0,\ \mathbf{e}_i^{\mathsf{T}}\mathbf{p} = 0\ , \tag{15}$$

see, e.g., [Nocedal and Wright 2006]. This more relaxed condition stipulates convexity for $E(\mathbf{x})$, and thus stability of the system, on the subspace orthogonal to the generalized coordinate $\mathbf{e}_i$. Along $\mathbf{e}_i$, however, it permits negative curvature in the energy. For sufficiently small deviations around the rest pose, $\mathbf{H}(\mathbf{x}) > 0$ will hold in any case such that any $\mathbf{n}_i(t)$ represents an equilibrium state for the load $\mathbf{f}^{ext}(t)$. For larger deformations, on the other hand, the loaded system might be unstable on $\mathbf{n}_i(\mathbf{x})$, but limited to only one direction, $\mathbf{e}_i$. Being slightly less restrictive regarding the second-order condition is a crucial aspect of our formulation, as it ensures continuity of $\mathbf{n}_i(t)$ for cases with non-monotonic force magnitude. Two examples for this are presented in Fig. 4 and discussed in Sec. 4.2. The bi-stable switch (*left*) and the flexible truss (*right*) both exhibit a decrease in force magnitude along the shown modes, implying negative stiffness (regions highlighted *red*). Hence, the corresponding part of the trajectory would not belong to the solution space of (14), as it is not a *stable* equilibrium state of the unconstrained system. Nonetheless, it carries physical meaning: it represents the path the quasi-static system would travel if it were pushed past the point where $\mathbf{H}$ becomes indefinite.

Modal Forcing. As long as $E(\mathbf{x})$ remains convex, our formulation can be interpreted as follows: for any given parameter t, the state of the system must be such that the internal elastic forces are collinear with the corresponding eigenmode. Consequently, any point along a nonlinear compliant mode corresponds to a static equilibrium configuration for an externally applied *modal force* of some magnitude. Interestingly, the idea of modal forcing has already been used by Sifakis and Barbic [2012] to define modal derivatives at the origin. While they did not attempt to compute nonlinear modes, they define a trajectory through a simple force equilibrium condition, whereby the force direction is given through a linear combination of several eigenvectors. For the particular choice of using only one eigenvector as basis of the force direction, this defines a function for displacement $\mathbf{u} = \mathbf{u}(\lambda)$ through the condition

$$\nabla E(\mathbf{X} + \mathbf{u}(\lambda))) - \lambda \mathbf{e}_i = 0. \tag{16}$$

For sufficiently small deviations with $\mathbf{H}(\mathbf{X} + \mathbf{u}) \geq 0$, our formulation could also be interpreted as a reparameterization of this curve, using the directional displacement t instead of the force magnitude. However, when $\mathbf{H}(\mathbf{X} + \mathbf{u})$ becomes indefinite, the picture changes.

Relying only on equilibrium conditions leaves physically unstable configurations as part of the solution space. We illustrate this point on a slender beam (Fig. 3), for which we find that the 13^{th} eigenmode corresponds to axial compression. With increasing load, the beam will ultimately buckle, and our formulation correctly captures this behavior (Fig. 3, *bottom right*). On the other hand, when neglecting second-order optimality conditions, equation (16) permits solutions characterized by pure compression of the beam (*top right*)—which is neither energetically favourable, nor physically feasible.

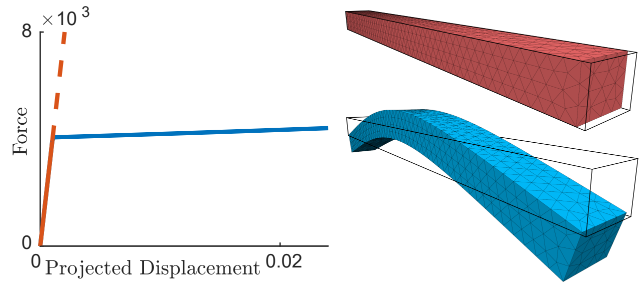

Fig. 3. Slender beam under axial compression. Unstable equilibrium configuration (*top right*) and the stable equilibrium resulting from our formulation (*bottom right*) obtained at a projected displacement of $t = 0.0068$. *Left:* Force plot for trajectories leading up to the configurations. The *dashed line* represents an unstable path.

Alternatively, physically *stable* equilibrium states for a system with gradually increasing external load can be computed through a conventional nonlinear FEM analysis. However, the mapping $\mathbf{u}(\lambda)$ is not guaranteed to be unique. Fig. 4 demonstrates two cases where the force magnitude does not increase monotonically with increasing deformation, leading to a discontinuity in $\mathbf{u}(\lambda)$ when the load is gradually increased. This issue is of course not limited to modal forces, but occurs with any choice of force direction. In our approach, the problem is effectively eliminated by using the directional displacement for parameterization. We will comment on this in more detail in Sec. 4.2.

4 RESULTS

We evaluated our method for computing nonlinear compliant modes on a set of examples that we describe in this section. We begin with a simple case that highlights qualitative and quantitative differences between linear eigenmodes and our nonlinear compliant modes. Besides visual results for simulation runs and physical experiments, we also show plots of energy, force, and stiffness as a function of *projected displacement*, i.e., a generalized displacement measure equivalent to the compliant mode parameter $t = \mathbf{e}_i^{\mathsf{T}}\mathbf{M}\mathbf{u}$.

4.1 Comparison to Linear Eigenmodes

We start our analysis by comparing linear eigenmodes and nonlinear compliant modes for a thin sheet, modeled using discrete shells [Grinspun et al. 2003]. The comparisons shown in Fig. 2 illustrate that our nonlinear compliant modes differ substantially from their linear counterparts on both qualitative and quantitative levels.

The nonlinear modes generally exhibit large bending deformations where linear modes are dominated by in-plane deformation. As a notable qualitative difference, the uniaxial bending mode that our method produces is clearly not predicted by the linear eigenstructure; see Fig. 2, *column 3*. A closer investigation shows that the corresponding linear mode induces a saddle-shaped bending deformation, i.e., a state of non-zero Gaussian curvature with a mix of in-plane stretching and compression. These compressions manifest as negative eigenvalues in $\mathbf{H}$, indicating the vicinity of a bifurcation. Instead of tracking this unstable equilibrium path, our method automatically follows the branch leading to stable constrained minima in the form of quasi-isometric uniaxial bending.

On a quantitative level, as shown in Fig. 2 (*column 4*), the elastic energy along linear eigenmodes is generally significantly higher than for their nonlinear counterparts, and differences grow rapidly with increasing parameter value. The reason for this discrepancy is that, instead of inducing bending, linear modes create in-plane deformations even if they are orthogonal to stretching at the origin.

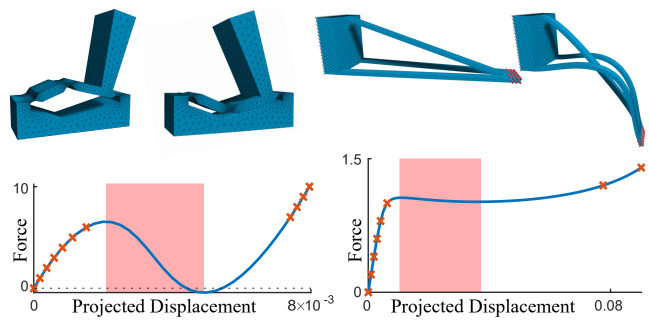

Fig. 4. Conventional nonlinear simulation with incremental loading compared to nonlinear compliant modes for cases with non-convex energy. *Left:* bistable switch, *right:* flexible truss with fixed boundary at the base and local restriction of the load to the tip on the far right (*red nodes*). The force directions are given by the linear eigenmodes, matching an activation motion for the switch and a gravitational load for the truss. Gradually increasing the force leads to a disconnected path (*red crosses* represent discrete steps), while the linear constraint in our formulation reveals the entire deformation path (*blue line*). *Red shading* indicates regions where the configurations exhibit an indefinite Hessian, and can thus not be reached with the unconstrained problem (14), irrespective of the loading strategy.

4.2 Comparison to Gradual Loading: Modal Forcing

In Section 3.5 we have discussed the connections and distinctions between our formulation and variations of modal forcing. Here we showcase the practical implications on two examples. To this end, we compare our method to nonlinear FEM analysis, which amounts to computing the response of an elastic object to an external load by solving the unconstrained minimization problem (14). In a traditional workflow, a load $\mathbf{f}^{\text{ext}}(t)$ would be specified manually by an expert user. While for some applications the forces acting on a structure are known a priori, in other cases load scenarios are more difficult to obtain. In particular, when the goal is to discover the nonlinear motion paths a structure can undergo easily, and conversely, which deformations it resists, determining appropriate loads manually can quickly become impractical. In such situations, linear eigenmodes are a useful and convenient way of defining meaningful force directions for deformation analysis. This idea is shared between our formulation and modal forcing. In the examples shown in Fig. 4 we set $\mathbf{f}^{\text{ext}}(t) = \lambda(t)\mathbf{e}_i$ to allow for a direct comparisons, though it is important to note that the following observations apply equally to any choice of $\mathbf{f}^{\text{ext}}(t)$.

The nonlinear compliant modes presented in Fig. 4 (*bottom, blue lines*) exhibit a non-monotonic force magnitude. Analyzing the same load scenario using (14) with the particular choice of $\lambda(t) = ct$, $c \in \mathbb{R}, c > 0$, i.e. applying a gradually increasing force, yields identical results initially (*red crosses*), for as far as $E(\mathbf{x})$ remains convex. Past that point, however, the system response exhibits a jump, and intermediate states cannot be easily examined. This notably includes the second equilibrium state of the bistable switch (*left*). A more elaborate choice of $\lambda(t)$ could allow to analyze further portions of the motion, e.g., by gradually *decreasing* the load again. However, certain regions of the deformation path cannot be reached either way: the red shading in the plots in Fig. 4 marks regions where the system Hessian is indefinite, i.e., the energy $E(\mathbf{x})$ is nonconvex, as indicated by the negative slope of the force magnitude. The configurations in those regions are not solutions of the unconstrained minimization problem (14), but can be analyzed using the constrained optimization problem (7) we propose.

Having investigated the properties of nonlinear compliant modes relative to linear eigenmodes and conventional FEM simulation, we now evaluate the potential of our method for analysis and design of real-world flexible structures.

4.3 Prismatic Flexures

Thanks to their high precision, low wear, and scaling capacity, compliant mechanisms are becoming an increasingly interesting replacement for their rigidly articulated counterparts. Since nonlinearity is a crucial aspect of functionality for compliant mechanisms, linear analysis is often inaccurate or even misleading.

As a case in point, we study the design of a prismatic flexure element that was recently proposed as a building block for modular compliant mechanisms [Rommers et al. 2021]. This element, shown in Fig. 5, is designed to allow bending of its axial wall, while the two other walls offer increased rigidity to lateral bending and twisting. Linear eigenanalysis seems to confirm this design intent, with the first non-rigid mode indicating a compliant direction for axial bending while the second mode, corresponding to lateral bending, is several times stiffer. Our nonlinear analysis, however, shows that the second mode (Fig. 5, *dashed red curve*) exhibits a drop in stiffness for larger deformations due to buckling of its axial wall. This decrease in lateral stiffness, completely missed by linear analysis, can translate into unexpected failure when using this element in larger assemblies.

Based on this observation, we create a modified design with two smaller prisms that provide additional support in the middle of the axial wall. While this modification does not prevent buckling altogether, it effectively shifts the instability to higher, energetically less favorable frequencies. Our nonlinear analysis shows that the first compliant mode remains largely unchanged (Fig. 5, *blue curve*), whereas the second mode shows largely improved load-bearing capacity (*red curve*). This prediction is confirmed by our experiments on 3D-printed prototypes.

Spherical Joint. As an extension of the previous example, we study a compliant spherical joint design by Rommers et al. [2021], consisting of a quasi-rigid end effector and a set of prismatic flexures; see

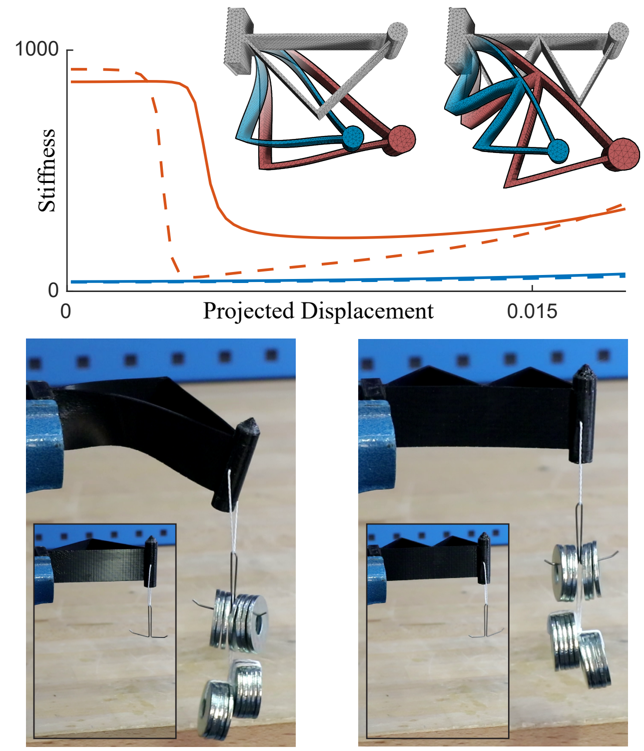

Fig. 5. Two designs for a prismatic flexure. *Top*: Rest state (*grey*) and predicted deformations for the first linear eigenmode (*red*) and nonlinear compliant mode (blue) for a given applied load. The plot shows stiffness for the compliant modes corresponding to axial bending (*blue*) and lateral bending (*red*) for Design A (*dashed*) and Design B (*solid*), respectively. *Bottom*: load bearing tests on physical prototypes.

Fig. 6. Our nonlinear analysis identifies two compliant modes that correspond to lateral rotations of the end-effector. Comparisons with a physical prototype show good agreement between our predictions and the real-world behavior through a large range motion.

As can be seen from the stiffness plot in Fig. 6, the next compliant mode, corresponding to translation along the axis of the end effector, is roughly five times stiffer initially (*yellow curve*). For larger deformations, however, the plot shows a highly asymmetric behavior with slowly increasing stiffness for pulling (positive displacement) but a sudden drop for pushing (negative displacement). A closer investigation reveals that this softening occurs when the structure *escapes* the pushing forces by switching into one of the rotation modes. Both softening and asymmetry are phenomena that are beyond the limits of linear analysis.

4.4 Topology-optimized Joints

Topology optimization is a powerful tool for generating designs in which material is distributed in mechanically optimal ways. While the goal is typically to maximize the stiffness to weight ratio, topology optimization can also be used to maximize rigidity for some deformations while achieving flexibility for other directions. We study applications of our method in this context on two compliant joint designs recently proposed by Koppen et al. [2022]. Both designs, shown in Fig. 7, were generated using the SIMP method [Bendsøe and Kikuchi 1988] based on linear elasticity. The intent of *Design A* (Fig. 7, *top row*) is to emulate a traditional universal joint by offering flexibility for lateral rotations (i.e., bending) while strongly resisting axial rotations (i.e., twisting). In contrast, *Design B* (Fig. 7, *bottom row*) is meant to enable twisting while strongly resisting bending. Linear analysis shows that the optimized designs fulfill these objectives for small deformations. Our nonlinear analysis partly confirms this prediction for larger displacements but also indicates some important limitations. While the first two compliant modes for *Design A* produce large bending deformations as expected, the third mode resists twisting only up to a certain angle where the buckling of a strut leads to a complete loss of stiffness. For *Design B*, our analysis shows a nonlinear increase in stiffness for twisting, ultimately limiting the feasible range of motion for this design.

4.5 Multistability

Multistability is a nonlinear phenomenon that can be exploited to create flexible structures with multiple discrete states. Here we investigate a basic implementation of this concept in the form of a bistable switch meant to exhibit two distinct equilibrium states. Analyzing the initial design shown in Fig. 1 (*top left*) with our method identifies switch activation as the first compliant mode. As can be seen from the force-displacement plot, the second compliant mode, corresponding to twisting of the lever, is already several times stiffer. More importantly, however, the force-displacement plot reveals that the initial design of the switch is dysfunctional: instead of exhibiting a second equilibrium point, the force along the activation mode is monotonically increasing. We argue that this design flaw, which is confirmed by the physical prototype (Fig. 1, *top right*), is difficult to detect a priori as it is not visible in the linear analysis. Our method allows us to identify such problems before any prototype is built. We use the insight gained from our nonlinear compliant modes to create an improved design in which a steeper rest angle allows for more vertical travel of the center flexure (Fig. 1, *bottom right*). As can be seen in the force plot, this second design iteration now exhibits the desired second equilibrium point, translating into a working prototype with the intended bistable behavior.

4.6 Structured Materials

Through precisely architected microstructures, mechanical metamaterials enable local control over their macro-mechanical properties. Besides this local influence, however, material structure can also shape the global deformation behavior in complex ways. We investigate the potential of our method for analysis and design in this context on two examples.

We first study the deformation behavior of a laser-sintered cylinder whose quasi-rigid end caps are connected by a set of axial rods[2]. Our analysis reveals three compliant modes that are orders of magnitude softer than the next stiffer mode. Two of these modes correspond to shearing deformation between top and bottom faces (Fig. 8,

[2]The radial rods are not physically connected to the axial ones and omitted in our simulation for simplicity

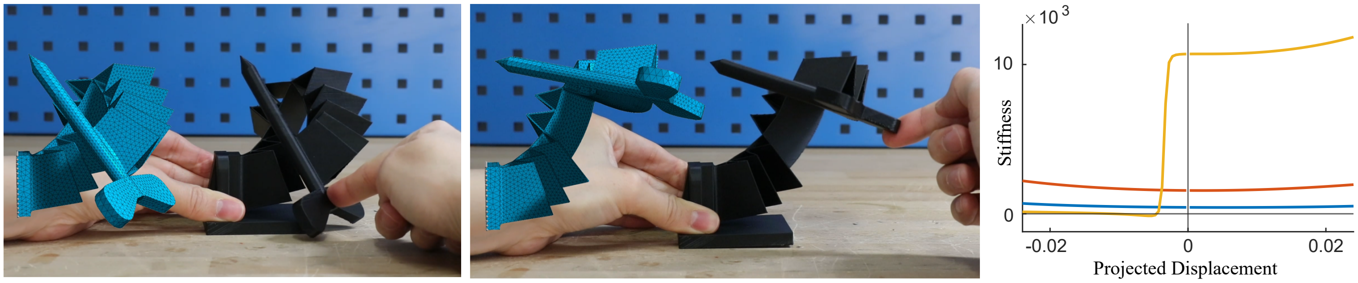

Fig. 6. A compliant mechanism emulating a conventional spherical joint. Our nonlinear analysis identifies two compliant modes corresponding to lateral rotations of the end-effector in orthogonal directions (*left* and *middle*). *Right*: stiffness plot for rotation modes (*blue* and *red*) and a third mode (*yellow*) corresponding to axial translation along the end-effector.

top row), whereas the third mode describes a nonlinear twist (*bottom row*). Fig. 8 shows that there are significant differences between our nonlinear compliant modes (*middle column*) and the corresponding linear eigenmodes (*right column*), with the linear modes showing unrealistic axial stretch for shearing and radial expansion for twisting. The nonlinear compliant modes, by contrast, are in good agreement with the experimental observations.

In a second example of structured materials, we investigate two beams with regularly-spaced incision patterns. The incisions are placed orthogonal to the beam axes and rotated by 180 degrees and 90 degrees for *Design A* and *Design B*, respectively. To account for contact between neighboring lamella during deformation, we create a tetrahedral mesh for the bounding box that conforms to the gaps. For each gap element we set up a penalty term that strongly resists compression beyond a threshold value of 98% of the initial volume. We also use this example to investigate our extension for locally-restricted modes (see Appendix A) and allow forces to be applied only at the two ends of the beam.

For both designs, our method identifies two compliant modes corresponding to low-frequency bending. As can be expected from their incision patterns, *Design A* exhibits anisotropic bending resistance whereas *Design B* behaves isotropically. Interestingly, both designs exhibit strong rigidity to twisting.

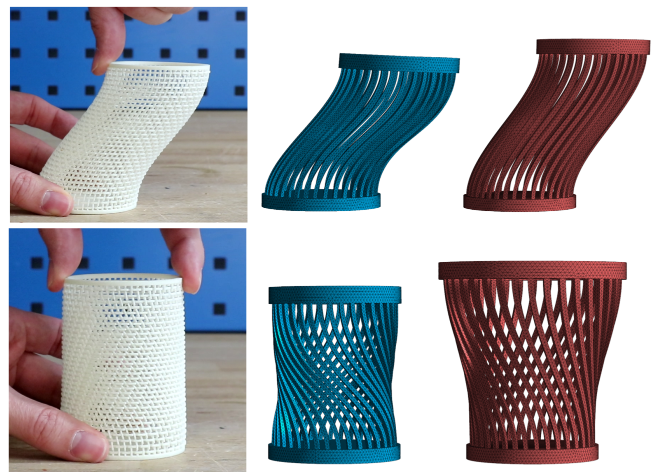

Fig. 8. Structured cylinder. Physical prototype (*left*), nonlinear compliant mode (*middle*), and linear eigenmode (*right*) for shearing (*top*) and axial twist (*bottom*) modes.

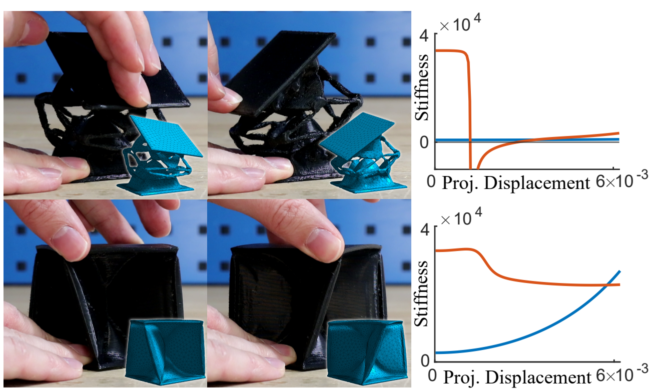

Fig. 7. Topology-optimized compliant joints. Design A (*top row*) is meant to be rigid for twisting but flexible for bending. Design B (*bottom row*) is intended to be flexible for twisting but rigid for bending. *Top right*: stiffness plots for compliant modes corresponding to bending (*blue*) and twisting (*red*). *Bottom right*: stiffness plots for compliant modes corresponding to twisting (*blue*) and axial compression (*red*).

As can be seen in Fig. 9, *column 3*, the bending modes initially show low rigidity but suddenly stiffen noticeably. Investigation of the simulation results shows that this stiffening occurs once a complete chain of contact between lamellas has formed (*column 1* and *2*)—a clearly nonlinear phenomenon that is captured faithfully by our method.

Besides the differences in bending behavior induced by the different incision patterns, *Design B* also leads to significantly higher stresses for larger bending deformations; see Fig. 9, *column 4*. For our 3D printed prototypes, these stress concentrations led *Design B* to break during manipulation whereas *Design A* remained intact. It should be emphasized that neither the contact-induced stiffening nor the difference in peak stresses are predicted by the linear eigenmodes.

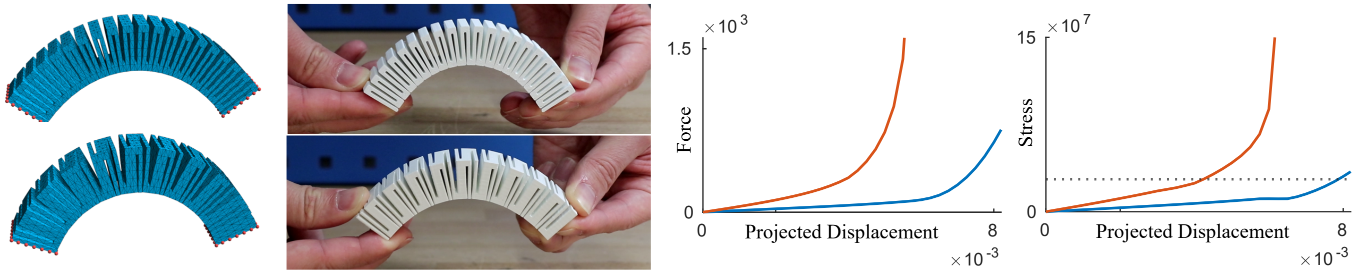

Fig. 9. Elastic beams structured with subsequent incisions rotated by 180 degrees for Design A (*top*) and 90 degrees for Design B (*bottom*) around the long axis. Nonlinear compliant modes for bending (*column 1*) and corresponding prototype behavior (*column 2*). Vertices with active displacement constraints are indicated in *red*. Plots showing stiffness (*column 3*) and von-Mises stress (*column 4*) for Design A (blue) and Design B (red). The dashed line indicates the yield threshold for the PLA material used for 3D-printing.

4.7 Implementation & Statistics

Except for the initial thin sheet example simulated using discrete shells, we used a standard finite element implementation based on linear tetrahedra with a Neo-Hookean material model for all other examples. Constitutive parameters were set according to specifications from the material manufacturer. We used polyamide 12 for the laser-sintered cylinder, TPU for the 3D-printed prismatic flexures, the bistable switch, and the topology-optimized joints, and ASA for the 3D-printed spherical joint and structured beams.

We use the Intel MKL Pardiso library to solve the linear system via sparse direct square-root-free Cholesky factorization; eigenvectors are computed using the shift-and-invert mode of the Spectra library, which operates on sparse matrices. Otherwise we rely on the Eigen library for linear algebra and matrix manipulation. As can be seen from Table 1, computing one configuration along a nonlinear compliant mode takes in the order of 1 second most cases, and about 6 seconds for the cylinder, which is by far the most complex of our examples. The number of steps we used for computing each compliant mode ranges from 13 (*cylinder*) to 124 (*topology optimized joints*). Computation times for each step are comparable to the time it takes to solve a static equilibrium problem. Our Newton solver required around 5 iterations on average. Solving the linear system is the most costly operation, accounting for about half of the computation time in all cases.

Table 1. Statistics and timings for the different examples. The number of steps used for computing the compliant modes ranges from 13 (*cylinder*) to 124 (*topology optimized joints*).

	Degrees of Freedom	Step Size	Time per Step average (s)
Prismatic Flexure A	15 597	2.5e-4	0.59
Prismatic Flexure B	17 322	2.5e-4	0.64
Spherical Joint	33 162	5.0e-4	1.35
Topology-opt. Joint A	17 796	5.0e-5	0.61
Topology-opt. Joint B	33 090	5.0e-5	1.18
Bistable Switch A	15 783	2.5e-4	0.72
Bistable Switch B	16 326	2.5e-4	0.99
Cylinder	86 076	1.0e-3	6.12
Beam A	10 080	2.5e-4	1.21
Beam B	11 760	2.5e-4	1.77
Truss	12 096	1.0e-3	0.52

5 CONCLUSIONS

We presented nonlinear compliant modes as a new approach for analyzing the finite-deformation behavior of flexible structures. Our formulation coincides with the linear eigenmodes for small deformations while naturally extending them to the nonlinear setting using energy minimization principles. While we believe that our results indicate the potential of nonlinear compliant modes, our method currently has several limitations that indicate opportunities for future research.

5.1 Limitations & Future Work

As for linear eigenvectors, our nonlinear modes are not independent of discretization and, in particular, coarse meshes can induce bias. While the dependence on mesh structure is, to a large extent, inherent to the specific discrete elasticity operators, spectral coarsening [Liu et al. 2019] could be a viable approach for reducing artefacts due to mesh resolution.

Our experiments indicate that nonlinear compliant modes are a promising tool for characterizing the large-deformation behavior of flexible structures. While our approach already enables simulation-based forward design, extending our formulation to inverse design modes—i.e., finding parameters that give rise to desired nonlinear modes—is an exciting research avenue for material design.

Our method requires the computation of eigenvectors. Fortunately, since we are only interested in a small number of low-energy modes (corresponding to the smallest eigenvalues), we can leverage sparse methods based on Arnoldi Iterations. While eigenmode computation with Spectra was not a limiting factor in our experiments, the method described by Yang et al. [2015] could be an interesting option if further acceleration was required.

Using the eigenvectors evaluated at the rest pose has proved to be a fruitful approach for defining the generalized coordinate for our nonlinear modes. For very large deformations, however, it can eventually lose its alignment with directions of low-energy deformation. For example, as rotations locally approach 90 degrees, stretching may eventually prevail over bending and twisting.

We have focused on static deformations with the goal of exploring and characterizing the intrinsic behavior of elastic structures undergoing large deformation. Nevertheless, extending our method to the dynamic setting is an interesting direction for future work. One promising option would be to build on the invariant manifolds concept by Shaw and Pierre [1991]: the system is reduced to two generalized coordinates for displacement and velocity along a given linear eigenvector, the remaining degrees of freedom are determined implicitly through dynamic equilibrium conditions. We believe that this approach presents an opportunity for applying our formulation in combination with optimization-based time stepping methods.

A MODE LOCALIZATION

To support locally-restricted modes in our formulation, we assign all nodes to either the active set $\mathcal{A}$ or the passive set $\mathcal{P}$ and compute localized linear eigenmodes $\mathbf{l}_i$ by asking that nodes $\mathbf{x}_p \in \mathcal{P}$ must have vanishing forces, i.e.,

$$\begin{bmatrix} \mathbf{H}_{\mathcal{A}\mathcal{A}} & \mathbf{H}_{\mathcal{A}\mathcal{P}} \\ \mathbf{H}_{\mathcal{P}\mathcal{A}} & \mathbf{H}_{\mathcal{P}\mathcal{P}} \end{bmatrix} \begin{bmatrix} \mathbf{l}_a \\ \mathbf{l}_p \end{bmatrix} = \begin{bmatrix} \sigma \mathbf{l}_a \\ \mathbf{0} \end{bmatrix} , \tag{17}$$

After block substitution, we obtain the system

$$\left(\mathbf{H}_{\mathcal{A}\mathcal{A}} - \mathbf{H}_{\mathcal{A}\mathcal{P}} \mathbf{H}_{\mathcal{P}\mathcal{P}}^{-1} \mathbf{H}_{\mathcal{P}\mathcal{A}} \right) \mathbf{l}_a = \sigma \mathbf{l}_a , \tag{18}$$

from which we compute the localized eigenvector using dense eigenvalue decomposition. We note that, unlike the sparse eigenvalue decompositions that we use for computing global eigenvectors, the cost of this dense operation rapidly increases with the size of the system, implying that the number of active vertices $\mathbf{x}_a \in \mathcal{A}$ must remain moderate.

REFERENCES

Jernej Barbič and Doug L. James. 2005. Real-Time Subspace Integration for St. Venant-Kirchhoff Deformable Models. *ACM Trans. Graph.* 24, 3 (July 2005), 982–990. https://doi.org/10.1145/1073204.1073300

Jernej Barbič, Funshing Sin, and Eitan Grinspun. 2012. Interactive Editing of Deformable Simulations. *ACM Trans. Graph.* 31, 4, Article 70 (July 2012), 8 pages. https://doi.org/10.1145/2185520.2185566

Martin Philip Bendsøe and Noboru Kikuchi. 1988. Generating optimal topologies in structural design using a homogenization method. *Comput. Methods Appl. Mech. Eng.* 71, 2 (1988), 197–224.

Gaurav Bharaj, David I. W. Levin, James Tompkin, Yun Fei, Hanspeter Pfister, Wojciech Matusik, and Changxi Zheng. 2015. Computational Design of Metallophone Contact Sounds. *ACM Trans. Graph.* 34, 6, Article 223 (Oct. 2015), 13 pages. https://doi.org/10.1145/2816795.2818108

Min Gyu Choi and Hyeong-Seok Ko. 2005. Modal warping: real-time simulation of large rotational deformation and manipulation. *IEEE Trans. Vis. Comput. Graph.* 11, 1 (2005), 91–101. https://doi.org/10.1109/TVCG.2005.13

Anders Eriksson and Arne Nordmark. 2019. Constrained stability of conservative static equilibrium. *Comput. Mech.* 64, 4 (01 Oct 2019), 1199–1219. https://doi.org/10.1007/s00466-019-01700-8

Lawson Fulton, Vismay Modi, David Duvenaud, David I. W. Levin, and Alec Jacobson. 2019. Latent-space Dynamics for Reduced Deformable Simulation. *Comput. Graph. Forum* 38, 2 (2019), 379–391. https://doi.org/10.1111/cgf.13645

Eitan Grinspun, Anil N. Hirani, Mathieu Desbrun, and Peter Schröder. 2003. Discrete Shells. In *Proc. ACM SIGGRAPH/Eurographics Symp. Comput. Animat.* (San Diego, California) *(SCA '03)*. Eurographics Association, Aire-la-Ville, Switzerland, 62–67. http://dl.acm.org/citation.cfm?id=846276.846284

Ruslan Guseinov, Eder Miguel, and Bernd Bickel. 2017. CurveUps: Shaping Objects from Flat Plates with Tension-Actuated Curvature. *ACM Trans. Graph.* 36, 4, Article 64 (July 2017), 12 pages. https://doi.org/10.1145/3072959.3073709

Fabian Hahn, Sebastian Martin, Bernhard Thomaszewski, Robert Sumner, Stelian Coros, and Markus Gross. 2012. Rig-Space Physics. *ACM Trans. Graph.* 31, 4, Article 72 (July 2012), 8 pages. https://doi.org/10.1145/2185520.2185568

Fabian Hahn, Bernhard Thomaszewski, Stelian Coros, Robert W. Sumner, Forrester Cole, Mark Meyer, Tony DeRose, and Markus Gross. 2014. Subspace Clothing Simulation Using Adaptive Bases. *ACM Trans. Graph.* 33, 4, Article 105 (July 2014), 9 pages. https://doi.org/10.1145/2601097.2601160

Klaus Hildebrandt, Christian Schulz, Christoph Von Tycowicz, and Konrad Polthier. 2011. Interactive Surface Modeling Using Modal Analysis. *ACM Trans. Graph.* 30, 5, Article 119 (Oct. 2011), 11 pages. https://doi.org/10.1145/2019627.2019638

Daniel Holden, Bang Chi Duong, Sayantan Datta, and Derek Nowrouzezahrai. 2019. Subspace Neural Physics: Fast Data-Driven Interactive Simulation. In *Proc. ACM SIGGRAPH/Eurographics Symp. Comput. Animat.* (Los Angeles, California) *(SCA '19)*. ACM, New York, NY, USA, Article 6, 12 pages. https://doi.org/10.1145/3309486.3340245

Jin Huang, Yiying Tong, Kun Zhou, Hujun Bao, and Mathieu Desbrun. 2011. Interactive Shape Interpolation through Controllable Dynamic Deformation. *IEEE Trans. Vis. Comput. Graph.* 17, 7 (2011), 983–992. https://doi.org/10.1109/TVCG.2010.109

Shobhit Jain and George Haller. 2022. How to compute invariant manifolds and their reduced dynamics in high-dimensional finite element models. *Nonlinear dynamics* 107, 2 (2022), 1417–1450.

Theodore Kim and Doug L. James. 2009. Skipping Steps in Deformable Simulation with Online Model Reduction. *ACM Trans. Graph.* 28, 5 (Dec. 2009), 1–9. https://doi.org/10.1145/1618452.1618469

S. Koppen, M. Langelaar, and F. van Keulen. 2022. A simple and versatile topology optimization formulation for flexure synthesis. *Mechanism and Machine Theory* 172 (2022), 104743. https://doi.org/10.1016/j.mechmachtheory.2022.104743

Bernd Krauskopf, Hinke M Osinga, Eusebius J Doedel, Michael E Henderson, John Guckenheimer, Alexander Vladimirsky, Michael Dellnitz, and Oliver Junge. 2005. A survey of methods for computing (un) stable manifolds of vector fields. *International Journal of Bifurcation and Chaos* 15, 03 (2005), 763–791.

Hsueh-Ti Derek Liu, Alec Jacobson, and Maks Ovsjanikov. 2019. Spectral Coarsening of Geometric Operators. *ACM Trans. Graph.* 38, 4, Article 105 (jul 2019), 13 pages. https://doi.org/10.1145/3306346.3322953

Luigi Malomo, Jesús Pérez, Emmanuel Iarussi, Nico Pietroni, Eder Miguel, Paolo Cignoni, and Bernd Bickel. 2018. FlexMaps: Computational Design of Flat Flexible Shells for Shaping 3D Objects. *ACM Trans. Graph.* 37, 6, Article 241 (Dec. 2018), 14 pages. https://doi.org/10.1145/3272127.3275076

Sebastian Martin, Bernhard Thomaszewski, Eitan Grinspun, and Markus Gross. 2011. Example-Based Elastic Materials. *ACM Trans. Graph.* 30, 4, Article 72 (July 2011), 8 pages. https://doi.org/10.1145/2010324.1964967

Jonàs Martínez, Jérémie Dumas, and Sylvain Lefebvre. 2016. Procedural Voronoi Foams for Additive Manufacturing. *ACM Trans. Graph.* 35, 4, Article 44 (2016), 12 pages.

Jonàs Martínez, Mélina Skouras, Christian Schumacher, Samuel Hornus, Sylvain Lefebvre, and Bernhard Thomaszewski. 2019. Star-Shaped Metrics for Mechanical Metamaterial Design. *ACM Trans. Graph.* 38, 4, Article 82 (July 2019), 13 pages. https://doi.org/10.1145/3306346.3322989

Vittorio Megaro, Jonas Zehnder, Moritz Bächer, Stelian Coros, Markus Gross, and Bernhard Thomaszewski. 2017. A Computational Design Tool for Compliant Mechanisms. *ACM Trans. Graph.* 36, 4, Article 82 (July 2017), 12 pages. https://doi.org/10.1145/3072959.3073636

Przemyslaw Musialski, Christian Hafner, Florian Rist, Michael Birsak, Michael Wimmer, and Leif Kobbelt. 2016. Non-linear Shape Optimization Using Local Subspace Projections. *ACM Trans. Graph.* 35, 4, Article 87 (July 2016), 13 pages. https://doi.org/10.1145/2897824.2925886

Jorge Nocedal and Stephen Wright. 2006. *Numerical optimization.* Springer Science, New York, NY, USA.

Zherong Pan, Hujun Bao, and Jin Huang. 2015. Subspace Dynamic Simulation Using Rotation-Strain Coordinates. *ACM Trans. Graph.* 34, 6, Article 242 (Oct. 2015), 12 pages. https://doi.org/10.1145/2816795.2818090

Julian Panetta, Abtin Rahimian, and Denis Zorin. 2017. Worst-case Stress Relief for Microstructures. *ACM Trans. Graph.* 36, 4, Article 122 (July 2017), 16 pages. https://doi.org/10.1145/3072959.3073649

Julian Panetta, Qingnan Zhou, Luigi Malomo, Nico Pietroni, Paolo Cignoni, and Denis Zorin. 2015. Elastic Textures for Additive Fabrication. *ACM Trans. Graph.* 34, 4, Article 135 (jul 2015), 12 pages. https://doi.org/10.1145/2766937

Jesús Pérez, Miguel A. Otaduy, and Bernhard Thomaszewski. 2017. Computational Design and Automated Fabrication of Kirchhoff-plateau Surfaces. *ACM Trans. Graph.* 36, 4, Article 62 (July 2017), 12 pages. https://doi.org/10.1145/3072959.3073695

Jelle Rommers, Volkert van der Wijk, and Just L. Herder. 2021. A new type of spherical flexure joint based on tetrahedron elements. *Precision Engineering* 71 (2021), 130–140. https://doi.org/10.1016/j.precisioneng.2021.03.002

R.M. Rosenberg. 1966. On Nonlinear Vibrations of Systems with Many Degrees of Freedom. Adv. Appl. Mech., Vol. 9. Elsevier, 155 – 242. https://doi.org/10.1016/S0065-2156(08)70008-5

Christian Schumacher, Steve Marschner, Markus Cross, and Bernhard Thomaszewski. 2018. Mechanical Characterization of Structured Sheet Materials. *ACM Trans. Graph.* 37, 4, Article 148 (July 2018), 15 pages. https://doi.org/10.1145/3197517.3201278

A. A. Shabana. 1990. *Theory of Vibration, Volume II: Discrete and Continuous Systems.* Springer, New York, NY, USA.

S.W. Shaw and C. Pierre. 1991. Non-linear normal modes and invariant manifolds. *J. Sound Vib.* 150, 1 (1991), 170 – 173. https://doi.org/10.1016/0022-460X(91)90412-D

S.W. Shaw and C. Pierre. 1993. Normal Modes for Non-Linear Vibratory Systems. *J. Sound Vib.* 164, 1 (1993), 85 – 124. https://doi.org/10.1006/jsvi.1993.1198

Eftychios Sifakis and Jernej Barbic. 2012. FEM Simulation of 3D Deformable Solids: A Practitioner's Guide to Theory, Discretization and Model Reduction. In *ACM SIGGRAPH 2012 Courses* (Los Angeles, California) *(SIGGRAPH '12)*. ACM, New York, NY, USA, Article 20, 50 pages. https://doi.org/10.1145/2343483.2343501

Mélina Skouras, Bernhard Thomaszewski, Peter Kaufmann, Akash Garg, Bernd Bickel, Eitan Grinspun, and Markus Gross. 2014. Designing Inflatable Structures. *ACM Trans. Graph.* 33, 4, Article 63 (jul 2014), 10 pages. https://doi.org/10.1145/2601097.2601166

Pengbin Tang, Jonas Zehnder, Stelian Coros, and Bernhard Thomaszewski. 2020. A Harmonic Balance Approach for Designing Compliant Mechanical Systems with Nonlinear Periodic Motions. *ACM Trans. Graph.* 39, 6, Article 191 (Nov. 2020), 14 pages. https://doi.org/10.1145/3414685.3417765

Nobuyuki Umetani, Jun Mitani, and Takeo Igarashi. 2010. Designing Custom-made Metallophone with Concurrent Eigenanalysis. In *Proc. Int. Conf. New Interfaces for Musical Expression*. Sydney, Australia, 26–30. https://doi.org/10.5281/zenodo.1177917

Nobuyuki Umetani, Athina Panotopoulou, Ryan Schmidt, and Emily Whiting. 2016. Printone: Interactive Resonance Simulation for Free-Form Print-Wind Instrument Design. *ACM Trans. Graph.* 35, 6, Article 184 (Nov. 2016), 14 pages. https://doi.org/10.1145/2980179.2980250

Christoph von Tycowicz, Christian Schulz, Hans-Peter Seidel, and Klaus Hildebrandt. 2013. An Efficient Construction of Reduced Deformable Objects. *ACM Trans. Graph.* 32, 6, Article 213 (Nov. 2013), 10 pages. https://doi.org/10.1145/2508363.2508392

Yin Yang, Dingzeyu Li, Weiwei Xu, Yuan Tian, and Changxi Zheng. 2015. Expediting Precomputation for Reduced Deformable Simulation. *ACM Trans. Graph.* 34, 6, Article 243 (Oct. 2015), 13 pages. https://doi.org/10.1145/2816795.2818089

Jonas Zehnder, Stelian Coros, and Bernhard Thomaszewski. 2016. Designing Structurally-Sound Ornamental Curve Networks. *ACM Trans. Graph.* 35, 4, Article 99 (jul 2016), 10 pages. https://doi.org/10.1145/2897824.2925888

Jiayi Eris Zhang, Seungbae Bang, David I. W. Levin, and Alec Jacobson. 2020. Complementary Dynamics. *ACM Trans. Graph.* 39, 6, Article 179 (Nov. 2020), 11 pages. https://doi.org/10.1145/3414685.3417819

Qingnan Zhou, Julian Panetta, and Denis Zorin. 2013. Worst-Case Structural Analysis. *ACM Trans. Graph.* 32, 4, Article 137 (July 2013), 12 pages. https://doi.org/10.1145/2461912.2461967

Received 02 February 2022; revised 03 August 2022; accepted 01 October 2022